1	Compaction of Porous H ₂ O-ice via Energetic Electrons
2	
3	Short Title: Compaction of H ₂ O-ice via Electrons
4	
5	Patrick R. Behr ^{1,2} , Patrick D. Tribbett ² , Tyler D. Robinson ² and Mark J. Loeffler ^{2,3}
6	
7	¹ Department of Physics and Astronomy, California State Polytechnic University,
8	Pomona, CA, 91768
9	
10	² Department of Astronomy and Planetary Science, Northern Arizona University,
11	Flagstaff, AZ, 86011
12	
13	³ Center for Materials Interfaces in Research and Applications, Northern Arizona
14	University, Flagstaff, AZ, 86011
15	
16	11 1 4 1 00/05/00 0 40
17	Updated: 08/05/20, 9:19 am
18	
19	

Abstract

Here we have investigated the degree to which energetic electrons cause structural changes in microporous H₂O-ice, using infrared and ultraviolet-visible spectroscopy as analytical tools. In these studies, we found that energetic electrons destroy both the dangling bond (DB) absorption bands, indicative of internal surface area, and the internal porosity of our samples. In addition, we find it takes about a factor of three higher fluence to decrease the internal pore volume by 63.2% than it does the internal surface area, which is likely because the surface area decreases by both destruction of the internal pores and also by smaller pores coalescing into large ones. Extrapolating our results to the interstellar medium, we estimate that the time need for these processes to occur is significantly shorter than the expected lifetime of a molecular cloud, leading us to speculate that future detections of the DB absorption bands or other indicators of porosity in the ISM will be relatively rare.

Keywords: Astrochemistry, Interstellar medium, Cosmic rays, Solid matter physics, Surface ices, Laboratory astrophysics, Spectroscopy

1. Introduction

64 65 66

67

68

69

70 71

72 73

74

75 76

77

78 79

Water vapor condensed onto cold (≤ 100K) surfaces forms microporous amorphous ice, which is commonly referred to as amorphous solid water (ASW) (Blackman & Lisgarten 1958; Mayer & Pletzer 1986). The intermolecular bonding of the water molecules located on the surface of ASW can differ from bonding in the bulk of the lattice, as the water molecules partially dangle off the surface into the pore structure. This difference, compared with the fully coordinated water molecule, can be seen with infrared spectroscopy through the presence of two absorption features located at 3696 cm⁻¹ and 3720 cm⁻¹ (Buch & Devlin 1991; Rowland, Fisher, & Devlin 1991). These two absorption bands have been assigned to the 3-coordinated (one free hydrogen bond) and 2coordinated water molecules (two free hydrogen bonds) and are referred to as dangling bonds (Buch & Devlin 1991). Laboratory studies have shown that these absorption bands are particularly sensitive to their environment. For instance, their intensity has a strong dependence on the ice temperature (Horimoto, Kato, & Kawai 2002; Rowland et al. 1991) and their peak position can shift significantly if another gas is adsorbed onto these dangling molecules (Buch & Devlin 1991; Chaabouni, Schriver-Mazzuoli, & Schriver 2000; Loeffler, Teolis, & Baragiola 2006; Raut et al. 2007a).

81 82 83

84

85

86

87

88 89

90

91 92

93

94 95

96

97

98

80

It is important to point out that these dangling bonds are more directly related to the internal surface area, which has been estimated from gas absorption experiments to be upwards of several hundred m² / g in microporous ice (Ayotte et al. 2001; Barnun et al. 1987; Horimoto et al. 2002; Mayer & Pletzer 1986), rather than the actual pore volume. Surfaces containing ASW are of interest from an astrochemical perspective, because these surfaces will have higher propensity to trap volatile species, which may alter the chemical evolution of the surface ice. Given that temperatures in the outer regions of our solar system and in the interstellar medium (ISM) are suitable to form ASW from ambient condensation of H₂O molecules, the absence of the dangling bond (DB) absorption features from remote sensing spectra is somewhat surprising. However, laboratory studies have shown that energetic ions can destroy these features fairly efficiently. possibly explaining their absence from remote sensing spectra (Dartois et al. 2013; Palumbo 2006; Raut et al. 2007b). These findings are qualitatively consistent with other laboratory approaches that more directly measure the sample porosity during ion irradiation (Palumbo 2006; Raut et al. 2008; Raut et al. 2007b), although it appears that the surface area decreases somewhat faster than pore collapse occurs (Raut et al. 2007b).

99 100 101

102

103

104

105

106

107

108

These previous laboratory studies have suggested that both the loss of surface area and porosity scales linearly with the ion's average stopping power (energy loss per unit path length) in the solid. However, the porosity studies also showed that the data was best fit by assuming there was a minimum stopping power needed to compact microporous ice of ~ 4 eV / Å (Raut et al. 2008), suggesting that only a specific range of cosmic ray ions will contribute to the compaction process in the ISM. This suggestion of a threshold for compaction is of interest from a fundamental perspective, as another structural effect, amorphization, appears to scale fairly linearly with the absorbed dose in

the sample even when including electrons and UV photons (Famá et al. 2010; Leto & Baratta 2003; Loeffler et al. 2020), giving no evidence for a threshold.

110111

112

113

114

115

116

117

118

119

120

121

122123

124

125

126

127

128129

130

131

132

133

134

135136

137

109

An adequate way to test whether there is a threshold for compacting microporous ice is to investigate these structural changes in ASW using keV electrons, which have an average stopping power that is about an order of magnitude lower than the estimated compaction threshold of 4 eV / Å. In addition, we expect keV electrons to serve as a reasonable analog for radiation processing via cosmic rays in the ISM. Both keV electrons and cosmic ray ions lose energy by producing thousands of ionizations and excitations as they pass through the solid, and many of these ionizations will ultimately produce secondary electrons, which deposit energy into the target medium, driving the observed changes. We note that energetic electrons have been used in a number of studies of H₂Oice, many of which have had an eye towards astronomical environments, to investigate processes such as radiolysis (Hand & Carlson 2011; Pan et al. 2004; Zheng, Jewitt, & Kaiser 2006), sputtering (Galli et al. 2018; Heide 1984; Meier & Loeffler 2020; Petrik, Kavetsky, & Kimmel 2006; Sieger, Simpson, & Orlando 1998), or amorphization (Dubochet & Lepault 1984; Heide 1984; Lepault, Freeman, & Dubochet 1983; Loeffler et al. 2020; Zheng, Jewitt, & Kaiser 2009). However, to date, there have been no laboratory studies on whether energetic electrons can alter physical properties of ASW, such as the surface area or porosity. Thus, we conducted a set of laboratory studies aimed at quantifying the destruction of the dangling bonds absorption bands and sample porosity in ASW induced by energetic electrons. Specifically, we irradiated thin films of amorphous H₂O-ice with 5 keV electrons. Irradiations were performed between 10 and 90 K, while the sample was monitored with infrared spectroscopy. For our most porous ices, we also utilized ultraviolet-visible (UV-Vis) spectroscopy, which enabled us to accurately assess the decrease in the sample's pore volume during irradiation. This combined analytical approach allows us to comprehensively study changes in the physical properties of ASW induced by energetic electrons, which will help to provide a more complete picture regarding the possibility of the existence of porous ice in interstellar ice mantles.

138139

2. Experimental Setup

140141142

143

144145

146147

148149

All experiments were performed inside a stainless steel ultra-high vacuum chamber on a thermal-radiation-shielded cryostat (Loeffler et al. 2020). The base pressure of the chamber was ~ 3×10^{-9} Torr, and inside the radiation shield it is estimated to be 10-100 times lower. Water-ice films were vapor-deposited at temperatures between 10 and 90 K onto the gold-coated surface of an Inficon IC6 quartz-crystal microbalance (QCM). The QCM measures the mass deposited per unit area, which can easily be converted to column density (molecules cm⁻²). The deposition rate was ~ 10^{15} molecules cm⁻² s⁻¹ (~3.5 Å s⁻¹) and in all experiments the column density of our H₂O-ice was $1.68 \pm 0.02 \times 10^{18}$ H₂O cm⁻².

After growth, samples were irradiated at their deposition temperature with 5 keV electrons, using an EGG-3103C Kimball Physics electron gun aimed at an incident angle of 12.5°. The electron beam was rastered uniformly over an area slightly larger than the sample surface to ensure that the entire ice was processed. The electron flux was typically $\sim 2 \times 10^{12} \, \mathrm{e^- \ cm^{-2} \ s^{-1}}$, which was determined using a Faraday Cup biased at +9V that could be moved in-line with the sample. During irradiation, although the Faraday Cup was moved away from the beam, we could still monitor the current using a thin wire that intersected the electron beam and was biased to -9V. The current during irradiation was stable, typically varying < 5%.

Analysis of the samples were performed before, during and after irradiation with UV-Vis and infrared reflectance (IR) spectroscopy. The UV-Vis measurements were made with an Avantes 2048XL fiber optic spectrometer over the wavelength range of 0.25 - 0.7 μm , at a resolution of 0.0015 μm . The IR measurements were made with a Thermo-Nicolet iS50 Fourier Transform Infrared Spectrometer (FTIR) over the range of 12,000 - 650 cm $^{-1}$ (~1.2 - 15.4 μm) at a spectral resolution set to 2 cm $^{-1}$. In both cases, the incident angle of the light was 37.5° with respect to the surface normal of our gold-mirror QCM. The resulting reflectance spectra are given by

$$R_{uv-vis} = \frac{I_{sample} - I_{dark}}{I_{reference} - I_{dark}} \qquad R_{IR} = \frac{I_{sample}}{I_{reference}}$$
(1)

where I_{sample} is the reflected intensity from the sample, $I_{reference}$ is the reflected intensity from our Gold-mirror reference, and I_{dark} is detector signal when the light source is blocked.

2.2 Data Analysis

Infrared spectroscopy and UV-vis spectroscopy

IR spectroscopy was used to probe the two- and three-coordinated dangling bond features located near 3720 and 3696 cm $^{-1}$ (Buch & Devlin 1991). To quantify the relative abundance of DBs present in our samples during electron irradiation, we first converted reflectance spectrum (1) into optical depth, - In R, and then used a 5th-order polynomial function to calculate a baseline continuum beneath the spectral bands. This non-linear baseline continuum was subtracted before integrating the total band area of both absorption bands. At temperatures \leq 30 K both DB absorptions could be confidently resolved, and thus we were able to measure the destruction of each absorption band using a multi-peak Gaussian fit.

While IR spectroscopy allows us to probe the porosity of H_2O -ice indirectly via analysis of the DB absorptions, the porosity of H_2O -ice can be directly determined in our experimental setup by extracting the sample thickness via modeling of the UV-Vis reflectance spectrum from the Fresnel equations (Raut et al. 2008; Teolis et al. 2007). As we directly measure the mass per unit area of our sample, we can easily determine the sample density by dividing by our derived sample thickness. As in previous work (Raut et al. 2008; Raut et al. 2007b), we then convert the density to sample porosity (P), where $P = 1 - \rho / \rho_c$, ρ is the density of the sample and ρ_c is the density of a fully compact film. In this study, we have used $\rho_c = 0.95 \pm 0.02$ g cm⁻³, which is the derived value for our most

highly irradiated samples. This value is consistent with that determined for compact H_2O ice (0.94 g cm⁻³; (Narten 1976). More details on our UV-Vis analysis is given in Appendix A

2.3 Stopping Power and Absorbed Energy Estimates

To compare our results to previous studies, we want to estimate the average energy transferred to our sample by the 5 keV electrons. As these electrons transfer mainly via inelastic collisions within the solid, we can quantify the energy transfer via the inelastic stopping cross section, S_e , which is related to the stopping power $(\frac{dE}{dx})$ through the relation $S_e = -\frac{1}{N}\frac{dE}{dx}$, where N is the number density of the material. To estimate this value, we averaged values of S_e from two publications (Ashley 1982; Francis et al. 2011) and those calculated from the NIST program ESTAR, which estimates the stopping power and ranges for electrons in different materials (Berger et al. 2005). These values are within 5% of one another at energies near 5 keV. As the electron travels through the sample, it loses energy and S_e increases. We estimated this increase, as well as the average S_e and absorbed dose in the sample using our iterative program described previously (Loeffler et al. 2020). These values are given in Table I.

A final aspect to consider is that in these experiments we are evaluating structural changes of an ASW sample, using both UV-Vis and infrared spectroscopy, which will probe our entire sample. Thus, we were careful to choose sample thicknesses where our electrons would pass entirely through the H_2O -ice. Given that our electrons pass through the entire sample, there is also the possibility that electrons will interact with our substrate, some being scattered back into the ice and others producing low-energy secondary electrons that can interact with the ice. While the latter effect is likely low (Loeffler et al. 2020), backscattering of electrons off gold has been measured to be somewhere between 30 and 50% for a sputter-cleaned gold sample in our electron energy range (Gomatic et al., 2008). Thus, assuming a worst-case scenario (i.e. 50% backscattering), the total energy absorbed in the sample may be underestimated by as much as 30%.

3. Results

3.1 Infrared Spectroscopy – DB absorptions under different growth conditions

Previous laboratory studies have shown that structure of vapor deposited H₂O-ice can depend on a number of different growth conditions, such as **the temperature** (Brown et al. 1996; Horimoto et al. 2002), deposition angle (Stevenson et al. 1999), growth rate (Sceats & Rice 1982) and even the type of deposition tube (Brown et al. 1996; Westley, Baratta, & Baragiola 1998). Thus, our initial experiments focused on studying how the DB absorption bands varied under different growth conditions within our experimental setup. Figure 1 shows samples deposited at an incident angle of 55° between 10 and 90 K, as well as ones deposited at 30 K via background deposition with and without the thermal-radiation shield attached. It is clear that DB absorption bands increase with decreasing growth temperature. Furthermore, the DB absorption bands in the background deposited

samples with the thermal-radiation shield removed were comparable to those samples deposited at 55°, yet both showed significantly larger DB absorption bands than background deposition when the thermal-radiation shield was attached. We note that the effect of the thermal-radiation shield on sample porosity has also been seen previously in studies on condensed CO₂ (Loeffler, Moore, & Gerakines 2016) and is likely due to the shield blocking molecules that are approaching the sample at very high angles of incidence. Regardless, based on these initial experiments we focused the majority of our irradiation experiments on samples deposited in a manner where the DB absorption bands were maximized (i.e. at either at 55° or via background deposition with the thermal-radiation shield removed).

3.2. Infrared spectroscopy - Stability of DB absorptions during electron irradiation

After vapor depositing H_2O -ice at an incidence angle of 55° , we irradiated the sample with 5 keV electrons, while monitoring the DB absorption bands with IR spectroscopy. Figure 2 shows the progression of the DB bands for an experiment performed at 50 K. It is evident that DB absorption bands decreased with increasing fluence and were reduced to the noise level at high fluences. We point out that these observed spectral changes are not a result of sputter removal of our sample, as at the highest fluence studied < 1% of our sample would be removed via sputtering (Meier & Loeffler 2020).

The decrease of the DB absorption bands shown in Figure 2 were quantified after extracting the baseline-corrected band area (see Section 2.2) and are shown in Figure 3 (top). The decrease in total DB band area is consistent with what is shown qualitatively in Figure 2, as at all temperatures the DB absorption bands are reduced to the noise level after an electron fluence of $\sim 1 \times 10^{16}$ electrons cm⁻². Furthermore, the rate of destruction of the DB absorption bands appears to have a somewhat weak dependence on temperature. For instance, the fluence needed to decrease the normalized DB band area by 1/2 is essentially the same, within error, below 50 K but is about 15% higher at 70 K and 30% higher at 90 K.

In addition to the total normalized DB band area, we also investigated the stability of each band during electron irradiation in cases where we could confidently resolve the two absorption features (≤ 30 K). Analysis of these two bands suggests that they appear to be destroyed at different rates with the two-coordinated (DB1; 3720 cm⁻¹) being removed before the three-coordinated (DB2; 3696 cm⁻¹) absorption band. More quantitatively, it took about twice as much fluence to destroy half of DB2 as compared to DB1. We saw similar results for our samples that were background deposited at 30 K (data not shown here).

3.3. UV-Vis spectroscopy – Porosity during electron irradiation

In addition to studying the samples with IR spectroscopy, we replaced the IR spectrometer with our UV-vis fiber optic setup to monitor the porosity of the sample during

electron irradiation. In these experiments, we focused on the background deposited samples, as they produced the highest-quality UV-Vis spectra.

After background depositing H₂O-ice, we irradiated the sample with 5 keV electrons at 30 K, while monitoring the sample's UV-Vis reflectance. The reflectance spectrum before and after irradiation, along with the corresponding model fit are shown in Figure 4. As H₂O-ice is transparent in this spectral region (Warren & Brandt 2008), the variation in the reflected intensity vs. wavelength is solely a result of interference between the gold substrate and the surface of the H₂O-ice (Heavens 1965). Before irradiation, we estimate that the sample thickness is 707 nm. After irradiation, the number of interference fringes seen in the spectrum decreases, indicating that the sample thickness has decreased. This qualitative assessment is supported by our UV-Vis analysis, which estimates the sample thickness is 528 nm after irradiation.

Figure 5 shows the porosity of our sample vs. electron fluence compared with the normalized band area of the DB absorptions for a sample produced via background deposition (Figure 1 top spectrum). The porosity decreases steadily during irradiation, and the sample fully compacts at high fluences. Interestingly, the porosity remains in the sample after the DBs have been destroyed, which is consistent with previous studies using heavy ions (Raut et al. 2007b). For instance, after a fluence of 1 x 10^{15} electrons cm⁻² the porosity has decreased by ~25% but the normalized DB band area has decreased by almost 80%.

4. Discussion

Laboratory studies investigating radiation processing of materials often investigate whether the rate and/or degree of sample alteration can be quantitatively related to some fundamental characteristic of the incident projectile, such as the total energy deposited in the sample or the stopping power of the incident projectile. These investigations have led to the observation that observed radiation chemistry induced by energetic particles in condensed gases is often driven by the total energy absorbed in the sample, regardless of whether the particle is a UV photon or energetic ion (Baratta, Leto, & Palumbo 2002; Gerakines, Moore, & Hudson 2004; Hudson & Moore 2001; Loeffler et al. 2005). A similar conclusion has also been observed on studies of the rate of amorphization of crystalline H₂O-ice (Famá et al. 2010; Loeffler et al. 2020; Strazzulla et al. 1992). However, this simple proportionality breaks down in the sputtering of condensed gases if a significant fraction of the energy transfer to the solid is through inelastic collisions, as is the case for keV – MeV ions and electrons (Baragiola et al. 2003; Brown, Augustyniak, & Lanzerotti 1980; Meier & Loeffler 2020). In these cases, the sputtering yield is shown to be quadratic or nearly quadratic with stopping power. Thus, as in these previous studies, it is also of interest to see whether the rate of decrease in the surface area and porosity of H2O-ice follow one of the above relations or another one entirely.

4.1 Comparison to Previous Studies Probing the Internal Surface Area

Studies investigating the stability of the DB absorption bands in pure H₂O-ice under energetic ion irradiation have shown that the DB absorption bands are destroyed down to the noise level (Dartois et al. 2013; Mejia et al. 2015; Palumbo 2006; Raut et al. 2007b), which is consistent with our experiments. Two studies have also investigated the relation between the DB destruction cross section and stopping power. Both studies showed that the relation between the two variables is approximately linear (Dartois et al. 2013; Mejia et al. 2015) with the best fit passing through the origin. Our experiments, where the average stopping power of the electrons is between 7 and 1000 times lower than the ions compiled in those previous studies, allow us to investigate whether this dependence extends to very low stopping powers.

To obtain a DB destruction cross section, previous studies have modeled the decrease in the DB absorption band area with projectile fluence using a single exponential decay function (Dartois et al. 2013; Mejia et al. 2015). Preliminary analysis of our data suggested that while this gave a reasonable fit to the data at higher irradiation temperatures, the agreement became progressively worse as the irradiation temperature was decreased. We speculate that the inadequacy of the single exponential fit at low temperatures is a result of the internal surface area decreasing through two main channels occurring at significantly different rates. A likely possibility, noted by Raut et al. (2007b), is that small pores are destroyed more quickly than the larger pores. This relationship can be described by two relatively simple differential equations:

$$\frac{dSA_S}{dF} = -\sigma_1 SA_S \tag{2}$$

$$\frac{dSA_l}{dF} = -\sigma_2 SA_l + \sigma_3 SA_s \tag{3}$$

where SA_s and SA_l are the surface area contained in the small and large pores, σ_1 is the cross section to remove the small pores, either by destruction or conversion to a larger pore, σ_2 is the cross section to destroy the large pores, σ_3 is the cross section to covert the smaller pores into larger ones, and F is the fluence.

Solving these integrals and combining them into an expression of the total surface area (SA_t) as a function of fluence, we obtain

$$SA_t(F) = A_1 e^{-\sigma_1 F} + A_2 e^{-\sigma_2 F}$$
 (4)

where $A_1=(1+\frac{\sigma_3}{\sigma_2-\sigma_1})SA_s(0)$ and $A_2=SA_l(0)-\frac{\sigma_3SA_s(0)}{\sigma_2-\sigma_1}$. An example of the model fit is shown in Figure 5, along with a single exponential fit. The derived cross sections from (4) are given in Table II.

We note that contribution of the first term in (4) is significantly less at 70 – 90 K, suggesting that the relative contribution of the small pores to the internal surface area decreases with increasing temperature. This is reasonable simply based on energetic

arguments, as smaller pores would be less favored at higher temperatures since larger pores minimize the surface area for a given volume. This also explains why the single exponential fit was better at higher temperatures, as the surface area is predominately in larger pores. We can also make an estimate for the relative amount of surface area contained in the smaller pores if either the majority of the smaller pores collapse rather than coalesce, $\sigma_3 << \sigma_1$, or if the majority of the small pores coalesce rather than collapse, $\sigma_3 \sim \sigma_1$. In either of these assumptions, we can solve for the coefficients given in (4), finding the smaller pores make up about 5 – 25 % of the total initial surface area and are most likely to exist in the samples with the highest porosity.

Given that the decrease in the DB absorption bands is best modeled with a double exponential decay curve with two distinctly different cross sections, it is not straightforward to compare our work with previous studies, which used a single exponential decay curve to fit the data. However, we can make a rough comparison by examining the fluence when the DB absorption band area drops by 1/e (or 63.2% are destroyed), as the reciprocal of this fluence value is similar to the cross section (σ) obtained if the data were fit with a single exponential decay curve. Those values are given in Table II and the sample background deposited at 30 K is compared with previous studies in Fig. 6 (top). The compilation of data is best fit with a simple power law fit of the form $\sigma = a (dE/dx)^x$, where $a = 32 \pm 11$ and $x = 1.35 \pm 0.05$, which is shown in Figure 6 (top). Attempts to fit the data using a linear relation, as has been done previously (Dartois et al. 2013), were only successful if we included a fairly large offset of ~6 eV / Å, suggesting that this power law relation may be a more realistic representation of the DB data. Whether the relation of x = 1.35 would be significantly different if a more robust analysis were performed on all the data given in Fig. 6 (top) is unclear but could be tested in future studies.

4.2 Comparison to Previous Studies Probing the Internal Pore Volume

Previous studies have shown that energetic ion irradiation can fully compact porous H_2O -ice (Raut et al. 2008; Raut et al. 2007b) and that the compaction occurs more slowly than the decrease in internal surface area (Raut et al. 2007b). Both of these findings are qualitatively consistent with our experiments.

In addition, Raut et al. (2008) determined that the cross section for compaction was linearly related to the average stopping power of the projectile, which was consistent with the Thermal Spike model (Szenes 1995) and the Modified Lattice Potential model (Watson & Tombrello 1985). However, they found that there appeared to be an offset in the data, suggesting that energetic particles with a stopping power below ~ 4 eV / Å would not fully compact the H_2O -ice. Given that our experiments utilize energetic electrons with an average stopping power well below this threshold (0.42 eV / Å; Table 1), yet still compact the H_2O -ice, we wanted to compare our results more quantitatively to see if another relation could be established.

To derive the destruction cross section, we fit the data in Figure 5 with a single exponential decay curve:

421
$$P(F) = P_0 e^{-\sigma_c F} + P_r \tag{5}$$

where P_0 is the initial porosity, P_r is any residual porosity in the sample at high fluences, σ_c is the compaction cross section and F is the fluence. The fit is shown in Figure 5, while the derived compaction cross section is shown in Table II. We note that the derived σ_c is the same as if we estimate it by evaluating the fluence at which 63.2% of the sample is compacted ($\sigma_c F = 1$), supporting the use of the single exponential fit to model the compaction. We note that the fluence needed to compact 63.2% of the sample is ~2.8 times larger than that needed to destroy an equivalent amount of DB absorption bands, which is essentially the same value (~3.0) that we estimate from previous work (see Raut et al. 2007, Figure 2). Furthermore, the 100 keV Ar⁺ used by Raut et al. (2007) deposits energy via both electronic and collisional processes and has a stopping power about ~100 times higher than our electrons, which only deposit energy via electronic processes. Thus, the similarity between the results from these two very different projectiles suggests that the rate at which the surface area precedes the collapse of the pore volume is relatively insensitive to the incident particle and how the energy is transferred to the solid.

In Figure 6 (bottom), we compare our derived compaction cross section with that reported for light ions in Raut et al. (2008). As with the DB data, the data is best fit with a power law relation but with a = 2.3 ± 1.5 and x = 1.74 ± 0.25 . This nearly quadratic relation between the compaction area and stopping power is similar to what has been reported for the relation between the sputtering of H_2O -ice and the electronic stopping power in experiments with keV and MeV ions and electrons (Baragiola et al. 2003; Brown et al. 1980; Meier & Loeffler 2020). The similar dependence to sputtering, rather than amorphization and radiation chemistry, may not be too surprising, as compaction, which is essentially the loss of internal pore space, occurs at the internal surfaces of our sample. Furthermore, it also suggests that rather than being driven by single collisions and thus related to the total energy deposited in the sample, compaction is likely a non-linear process, possibly driven by the overlap of pairs of excitations at the surface (Shi et al. 1995).

4.3 Astrophysical Implications

Our results show that the DB absorption bands and internal pore structure of microporous H_2O -ice can be destroyed by energetic electron irradiation at all temperatures studied (T \leq 90 K), which is consistent with previous studies using ion irradiation (Dartois et al. 2013; Mejia et al. 2015; Palumbo 2006; Raut et al. 2008; Raut et al. 2007b). Thus, we expect that microporous H_2O -ice present on the surface of an icy body will be compacted given a sufficient radiation dose, rendering the DB absorption bands undetectable

To make an estimate for the time (τ) needed to compact an interstellar ice mantle, we use the expression:

$$\tau^{-1} = 4\pi \sum_{Z} \int_{E_{min}}^{\infty} \boldsymbol{\sigma}_{c}(E, i) \Phi_{i}(E) dE$$
 (6)

where Z is the atomic number of the cosmic ray species, $\sigma_c(E, i)$ is the compaction cross section for the given species at a given energy, and $\Phi_i(E)$ is the cosmic ray flux. The compaction cross section can be estimated from our relation derived in Section 4.2, while the ion flux can be estimated from the expression given by Webber and Yushak (1983):

$$\Phi_i(E) = CE^{0.3}/(E + E_0)^3 (cm^2 s \ sr \ GeV^{-1}) \tag{7}$$

where C and E_0 can be determined using the analytical expressions developed by Bringa et al. (2007) and will vary depending on cosmic ray species. We set the lower limit of the integral in (6) to be the minimum velocity for a cosmic ray to escape a supernova remnant or $2mv^2$, where v is the shock velocity and is assumed to be ~5000 km/s (Bell 1978). We set the upper limit of the integral at ~10 GeV / amu, as this is the highest dE/dx value calculated by SRIM (Ziegler 2010). Integrating (6) for cosmic ray ions through Nickel, we find a compaction time of ~3.5 x 10^5 yrs, which is significantly shorter than the estimated lifetime (~ 10^7 yrs) for a molecular cloud (Blitz & Shu 1980). We note that this time is also much shorter than previous estimates (Raut et al. 2008), which is somewhat expected as we found that there was no threshold for compaction and that the compaction cross section had a non-linear dependence on the stopping power. Assuming the time for destruction of the DB bands is about a factor of three shorter than compaction time given above (Section 4.2), we find good agreement with the lower range of estimates given by Dartois et al. (2013).

We note that the relatively short time needed to compact porous H₂O-ice in the ISM should also effect the evolution of ice mantles and their ability to trap gas species that may adsorb on the surface. The loss of pore space should also inhibit the mixing and diffusion of the adsorbed molecules within the H₂O-ice mantle. This may be of particular interest for interstellar CO, as previous studies have shown that the 2152 cm⁻¹ CO absorption feature, which results from adsorption of CO onto the DB molecules (Fraser et al. 2004; Palumbo 1997), is lacking from interstellar spectra (Pontoppidan et al. 2003). These results may also be important for interpretation of the 2136 cm⁻¹ CO feature detected in multiple young stellar objects (Pontoppidan et al. 2003). While this is speculated to be from CO being trapped in collapsed pores of H₂O-ice through some annealing process (Fraser et al. 2004), it is possible that it could be formed during compaction of a mixed ice mantle caused by cosmic rays. The viability of this would need to be tested more thoroughly in the laboratory, as a previous study on a CO + H₂O-ice mixture made no mention whether this band was observed but also only partially compacted the sample (Palumbo 2006).

5. Conclusions

We have performed a set of experiments aimed at determining the degree to which structural changes in microporous H_2O -ice can be induced by energetic electrons. In these studies, we found that the DB absorption bands, indicative of the internal surface area of our samples, can be destroyed relatively quickly at all the temperatures studied (10-90 K), in agreement with previous studies that used energetic ions. Modeling the decrease in the DB absorption band area with fluence, suggests that the surface area decreases by both destruction of the internal pores but also by the smaller pores

coalescing into large ones. These results suggest that the internal pore volume will decrease more slowly than the internal surface area, which is supported by our UV-Vis results. Combining our data with previous studies, we determine that both ions and electrons, regardless of their stopping power, can destroy the dangling bond absorption bands and compact microporous ice. Furthermore, we find that the rate of compaction increases non-linearly with the stopping power, in a manner more similar to sputtering, rather than other processes, such as radiation chemistry and amorphization, which are typically explained by the total energy absorbed in the sample, rather than the rate of energy deposition.

Applying our results to extraterrestrial icy surfaces, we estimate that any surface containing microporous ice will lose its surface area and be compacted by energetic particles given enough time. More specifically, estimates made for the ISM suggest that the time needed to destroy the DB absorption bands and compact microporous ice is significantly shorter than the lifetime of a molecular cloud. Thus, future detections of the DB absorption bands in the ISM are expected to be relatively rare.

- Acknowledgements
- 525 This research was supported by NSF Grant # 1821919. Data can be found in Northern
- 526 Arizona University's long-term repository (https://openknowledge.nau.edu/5519/).

Appendix A – UV-Vis spectral analysis

A.1. Generation of Synthetic Spectra

To analyze our UV-Vis reflectance data, we generate synthetic reflectance spectra using the Fresnel equations (Heavens 1965), similar to what has been done in previous studies (Raut et al. 2008; Raut et al. 2007b). For a detailed description of the entire analytical approach, see work by Teolis et al. (2007).

As H₂O-ice is transparent in the spectral range of interest (Warren & Brandt 2008), we consider only the real part of the film's refractive index, which can be approximated by the Sellmeier equation:

$$n(\lambda) = \sqrt{\frac{A + (B\lambda)^2}{\lambda^2 - C^2}} \tag{8}$$

where λ is the wavelength and A, B, and C are the fitted Sellmeier coefficients. Using $n(\lambda)$ as input to our synthetic reflectance model, we generated theoretical spectra of the H₂O-ice $(R_{H_2O}(\lambda))$, for a given thickness (d), by taking the ratio of the total reflectance of the film and substrate (R_f) to the total reflectance from just the substrate (R_s) . R_s was derived from the optical constants for gold (Babar & Weaver 2015). Additionally, a factor was included in the model to account for the increased scattering that occurred after high irradiation fluences (σ_s) . This scattering is due to an increase in surface roughness and has been approximated using Rayleigh scattering (Born & Wolf 1970; Hapke 2012), since the surfaces roughness will be significantly smaller than the UV-Visible wavelengths used in this study. The synthetic spectra are formalized by:

$$R_{H_2O}(\lambda) = \frac{R_{f,s}}{R_s} (1 - \frac{\sigma}{\lambda^4})$$
 (9)

A.2. Synthetic Spectra Optimization

Synthetic spectra were optimized to the data using a Markov chain Monte Carlo (MCMC) implementation of Bayesian inference using emcee, which is an open-source software package based in Python (Foreman-Mackey et al. 2013). Bayes Theorem states that the conditional posterior probability distribution for some set of physical parameters (θ) given some set of data (x) is proportional to the prior probabilities of those parameters and the likelihood probability of the data given those parameters:

$$P(\theta|x) \propto P(x|\theta)P(\theta)$$
 (10)

where $P(\theta|x)$ is the posterior probability, $P(x|\theta)$ is the likelihood probability, and $P(\theta)$ is the prior probability. Using a modified Hasting-Metropolis algorithm, values for the model free parameters that generate the synthetic spectrum (Section A.1) are systematically explored to maximize the likelihood probability, which occurs when the

differences between the synthetic reflectance spectrum and the laboratory spectrum are minimized. A detailed description of the likelihood function and the parameter value selection algorithm can be found in Foreman-Macky (2013). The prior probabilities for each parameter limit the values that our parameters can take. These limits are based on the physical properties of the parameters (e.g., a thickness or length cannot be less than 0). Model free parameters with their descriptions and prior limits are shown in Table III. It should be noted that the scattering efficiency parameter was retrieved in log space to ensure exploration over two orders magnitude, and priors dictate that scattering efficiency cannot be greater than 100% for the minimum wavelength. Initial model conditions were based on best fit parameter values determined by visual fit inspection.

581 582 583

584

585

586587

588

589

590591

592

593

594

595 596

597598599600

601

572

573

574

575

576577

578

579

580

To our knowledge, this is the first use of Bayesian statistics to retrieve physical parameters in tandem with experimental astrophysical and astrochemical studies. Although this technique has not been previously employed for laboratory astrophysics, emcee and Bayesian statistics have been shown to be powerfully versatile in the astronomical community (Line et al. 2017; Line et al. 2015; Macintosh et al. 2014; Yan & Results for one of the model solutions are shown in Figure 7. In this Henning 2018). "corner plot", the marginalized probabilities for each individual parameter are shown on the diagonal axis. The distribution 16th, 50th, and 84th percentiles are shown above each marginalized posterior (i.e. the distribution mean and 1-σ uncertainties) that maximize the likelihood probabilities and these are subsequently used to produce the model spectra as shown in Figure 4. Off-diagonal axis corner plots show the two-dimensional marginalized posterior probability distributions for the vertical and horizontal axis parameters. These contour plots show correlations between two parameters, the most notable of which are the correlations between Sellmeier parameters. It should be noted, however, that these correlations are not over the entirety of parameter space as dictated by the prior limits.

602 References

- 605 Ashley, J. C. 1982, Rad Res, 89, 25
- 606 Ayotte, P., Smith, R. S., Stevenson, K. P., et al. 2001, J Geophys Res, 106, 33387
- 607 Babar, S., & Weaver, J. H. 2015, Appl Optics, 54, 477
- 608 Baragiola, R. A., Vidal, R. A., Svendsen, W., et al. 2003, Nuc Instr & Met B, 209, 294
- 609 Baratta, G. A., Leto, G., & Palumbo, M. E. 2002, Astron & Astrophys, 384, 343
- 610 Barnun, A., Dror, J., Kochavi, E., & Laufer, D. 1987, Phys Rev B, 35, 2427
- 611 Bell, A. R. 1978, Mon Not R Astron Soc, 182, 443
- 612 Berger, M. J., J.S. Coursey, J. S., Zucker, M. A., & Chang, J. 2005, in
- 613 (http://www.nist.gov/pml/data/star/index.cfm: NIST, Physical Measurement Laboratory)
- 614 Blackman, M., & Lisgarten, N. D. 1958, Adv Phys, 7, 189
- 615 Blitz, L., & Shu, F. H. 1980, Astrophys J, 238, 148
- Born, M., & Wolf, E. 1970, Principles of Optics (London: Pergamon Press)
- 617 Bringa, E. M., Kucheyev, S. O., Loeffler, M. J., et al. 2007, Astrophys J, 662, 372
- 618 Brown, D. E., George, S. M., Huang, C., et al. 1996, J Phys Chem, 100, 4988
- Brown, W. L., Augustyniak, W. M., & Lanzerotti, L. J. 1980, Phys Rev Lett, 45, 1632
- 620 Buch, V., & Devlin, J. P. 1991, J Chem Phys, 94, 4091
- 621 Chaabouni, H., Schriver-Mazzuoli, L., & Schriver, A. 2000, J. Low Temp Phys, 26, 712
- 622 Dartois, E., Ding, J. J., de Barros, A. L. F., et al. 2013, Astron & Astrophys, 557
- 623 Dubochet, J., & Lepault, J. 1984, J de Phys, 45, 85
- 624 Famá, M., Loeffler, M. J., Raut, U., & Baragiola, R. A. 2010, Icarus, 207, 314
- Foreman-Mackey, D., Hogg, D. W., Lang, D., & Goodman, J. 2013, Pub Astron Soc
- 626 Pac, 125, 306
- Francis, Z., Incerti, S., Karamitros, M., Tran, H. N., & Villagrasa, C. 2011, Nucl Instrum
- 628 Meth B, 269, 2307
- Fraser, H. J., Collings, M. P., Dever, J. W., & McCoustra, M. R. S. 2004, Mon Not R
- 630 Astron Soc, 353, 59
- 631 Galli, A., Vorburger, A., Wurz, P., et al. 2018, Plan Spac Sci, 155, 91
- 632 Gerakines, P. A., Moore, M. H., & Hudson, R. L. 2004, Icarus, 170, 202
- 633 Gomis, O., Leto, G., & Strazzulla, G. 2004, A&A, 420, 405

- 634 Hand, K. P., & Carlson, R. W. 2011, Icarus, 215, 266
- Hapke, B. 2012, Theory of Reflectance and Emittance Spectroscopy (2nd ed.:
- 636 Cambridge University Press)
- 637 Heavens, O. S. 1965, Optical properties of thin solid films (New York: Dover
- 638 Publications, Inc.)
- 639 Heide, H. G. 1984, Ultramicroscopy, 14, 271
- 640 Horimoto, N., Kato, H. S., & Kawai, M. 2002, J Chem Phys, 116, 4375
- 641 Hudson, R. L., & Moore, M. H. 2001, J Geophys Res, 106, 33275
- Lepault, J., Freeman, R., & Dubochet, J. 1983, J Micro Ox, 132, Rp3
- 643 Leto, G., & Baratta, G. A. 2003, Astron & Astrophys, 397, 7
- 644 Line, M. R., Marley, M. S., Liu, M. C., et al. 2017, Astrophysical Journal, 848
- 645 Line, M. R., Teske, J., Burningham, B., Fortney, J. J., & Marley, M. S. 2015, Astrophys
- 646 J, 807
- 647 Loeffler, M. J., Baratta, G. A., Palumbo, M. E., Strazzulla, G., & Baragiola, R. A. 2005,
- 648 Astron & Astrophys, 435, 587
- 649 Loeffler, M. J., Moore, M. H., & Gerakines, P. A. 2016, Astrophys J, 827, 98
- 650 Loeffler, M. J., Teolis, B. D., & Baragiola, R. A. 2006, Astrophys J, 639, L103
- 651 Loeffler, M. J., Tribbett, P. D., Cooper, J. F., & Sturner, S. J. 2020, Icarus
- Macintosh, B., Graham, J. R., Ingraham, P., et al. 2014, P Natl Acad Sci USA, 111,
- 653 12661
- 654 Mayer, E., & Pletzer, R. 1986, Nature, 319, 298
- 655 Meier, R. M., & Loeffler, M. J. 2020, Surf Sci, 691, 121509
- 656 Mejia, C., de Barros, A. L. F., Duarte, E. S., et al. 2015, Icarus, 250, 222
- 657 Moore, M. H., & Hudson, R. L. 2000, Icarus, 145, 282
- 658 Narten, A. H. 1976, J Chem Phys, 64, 1106
- 659 Palumbo, M. E. 1997, J Phys Chem A, 101, 4298
- 660 ---. 2006, Astron & Astrophys, 453, 903
- 661 Pan, X., Bass, A. D., Jay-Gerin, J.-P., & Sanche, L. 2004, Icarus, 172, 521
- 662 Petrik, N. G., Kavetsky, A. G., & Kimmel, G. A. 2006, J Phys Chem B, 2723
- 663 Pontoppidan, K. M., Fraser, H. J., Dartois, E., et al. 2003, A&A, 408, 981
- 664 Raut, U., Famá, M., Loeffler, M. J., & Baragiola, R. A. 2008, Astrophys J, 687, 1070

- Raut, U., Famá, M., Teolis, B. D., & Baragiola, R. A. 2007a, J Chem Phys, 127, 204713
- 666 Raut, U., Teolis, B. D., Loeffler, M. J., et al. 2007b, J Chem Phys, 126, 244511
- 667 Rowland, B., Fisher, M., & Devlin, J. P. 1991, J Chem Phys, 95, 1378
- Sceats, M. G., & Rice, S. A. 1982, in Water, a Comprehensive Treatise, ed. F. Franks
- 669 (New York: Plenum), 83
- Shi, M., Grosjean, D. E., Schou, J., & Baragiola, R. A. 1995, Nucl Instrum Meth B, 96,
- 671 **524**
- 672 Sieger, M. T., Simpson, W. C., & Orlando, T. M. 1998, Nature, 394, 554
- 673 Stevenson, K. P., Kimmel, G. A., Dohnalek, Z., Smith, R. S., & Kay, B. D. 1999,
- 674 Science, 283, 1505
- 675 Strazzulla, G., Baratta, G. A., Leto, G., & Foti, G. 1992, Europhys Lett, 18, 517
- 676 Szenes, G. 1995, Phys Rev B, 51, 8026
- Teolis, B. D., Loeffler, M. J., Raut, U., Famá, M., & Baragiola, R. A. 2007, Icarus, 190,
- 678 **274**
- 679 Warren, S. G., & Brandt, R. E. 2008, J Geophys Res, 113, D14220
- Watson, C. C., & Tombrello, T. A. 1985, Radiat Effects and Defects in Solids, 89, 263
- Webber, W. R., & Yushak, S. M. 1983, Astrophysical Journal, 275, 391
- 682 Westley, M. S., Baratta, G. A., & Baragiola, R. A. 1998, J Chem Phys, 108, 3321
- 683 Yan, F., & Henning, T. 2018, Nat Astron, 2, 714
- ⁶⁸⁴ Zheng, W., Jewitt, D., & Kaiser, R. I. 2006, Astrophys J, 639, 534
- ⁶⁸⁵ Zheng, W. J., Jewitt, D., & Kaiser, R. I. 2009, J Phys Chem A, 113, 11174
- Ziegler, J. F. 2010, Stopping and range of ions in matter SRIM2010 (available at
- 687 www.srim.org)

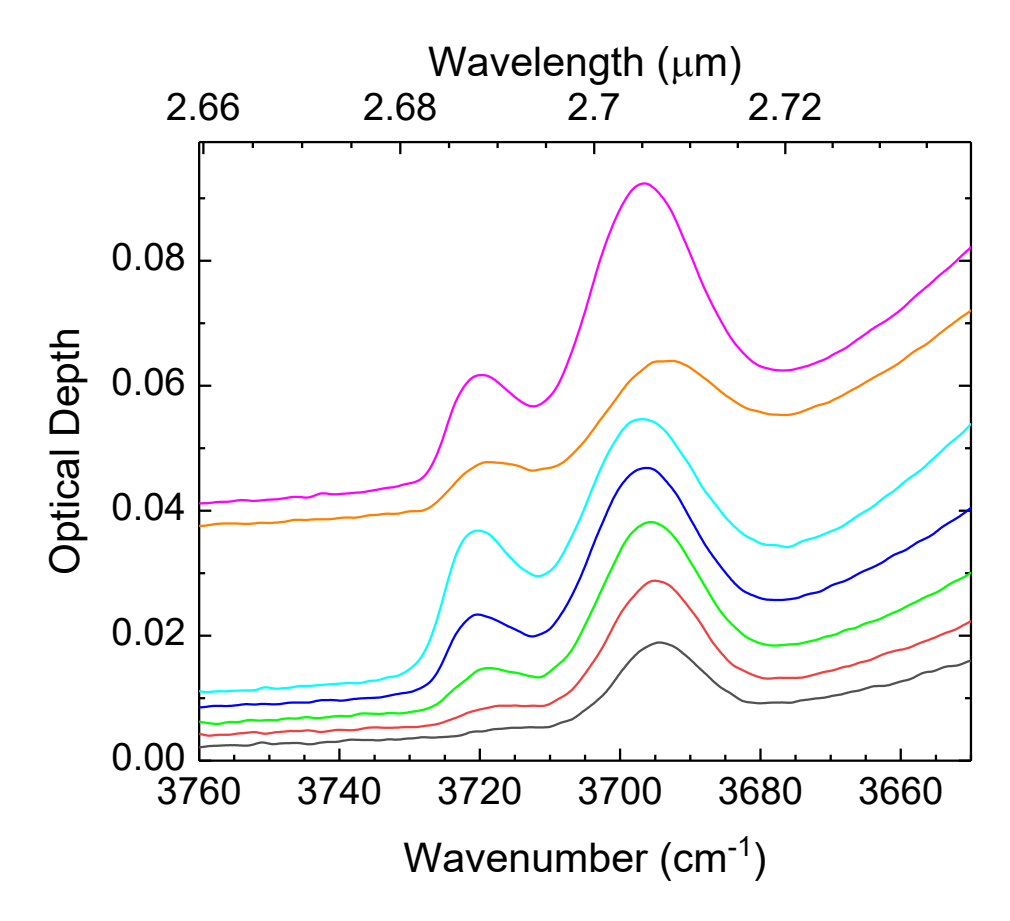


Figure 1. Infrared spectra of the dangling bond absorption bands for a $1.68 \times 10^{18} \text{ H}_2\text{O}$ cm⁻² sample for different deposition angles and temperatures. Spectra correspond to (from bottom to top): 90 K (55° deposition angle), 70 K (55° deposition angle), 50 K (55° deposition angle), 30 K (55° deposition angle), 10 K (55° deposition angle), 30 K (background deposit with thermal-radiation shield attached), and 30 K (background deposit with the thermal-radiation shield removed).

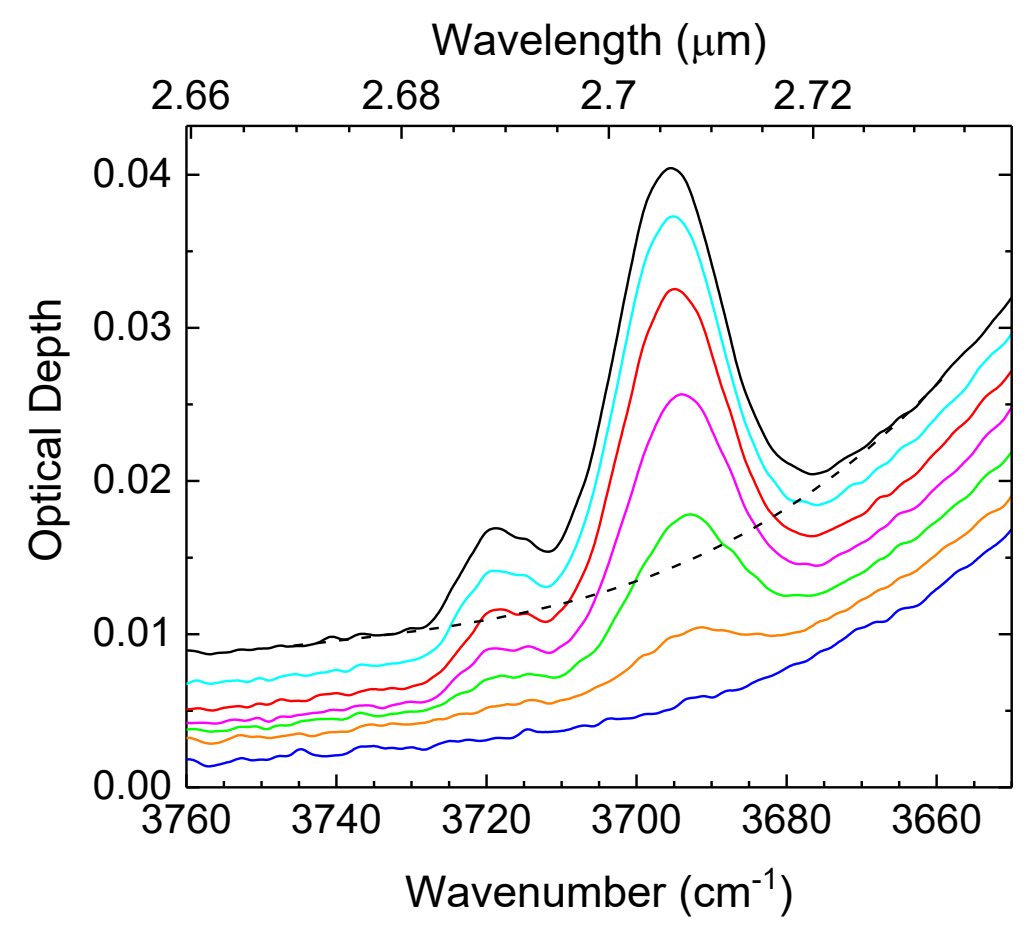


Figure 2. Infrared spectra of the dangling bond absorption bands for a 1.68 x 10^{18} H₂O cm⁻² sample deposited at 55° at 50 K during irradiation with 5 keV at 50 K. The spectra (from top to bottom) correspond to fluences (in units of 10^{14} electrons cm⁻²): 0, 0.25, 2.1, 3.7, 9.8, 26.6, and 109. The dotted line shows an example of our estimated continuum for our fresh film, which was derived using a 5th-order polynomial fit.

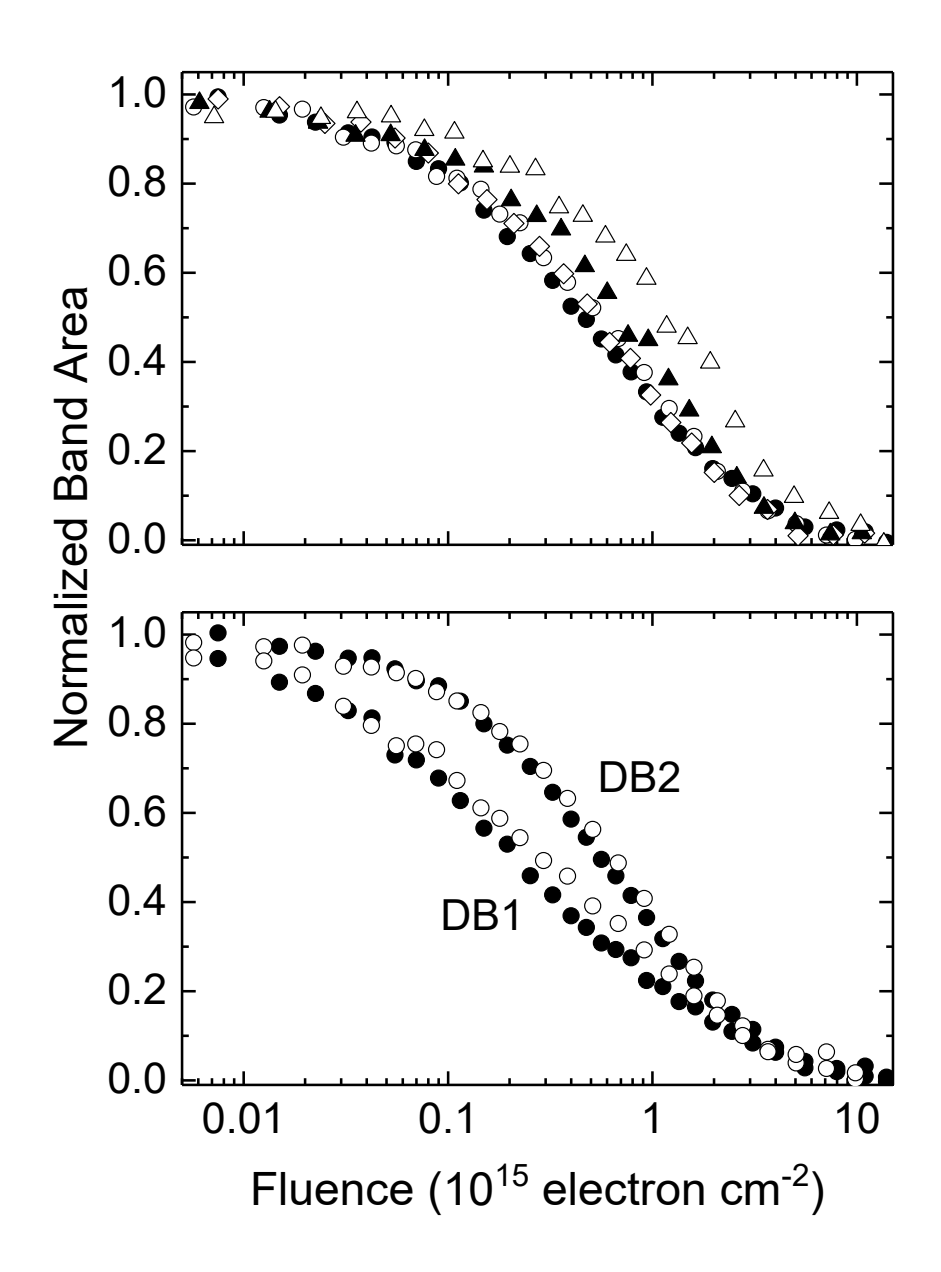


Figure 3. Normalized band area of the dangling bond absorption bands vs. electron fluence for 1.68 x 10^{18} H₂O cm⁻² samples deposited at 55° and irradiated with 5 keV electrons at temperatures between 10 and 90 K. Top: normalized band area of both dangling bond absorptions. Bottom: normalized band area for the individual 3720 cm⁻¹ (DB1) and 3696 cm⁻¹ (DB2) absorption bands. Symbols correspond to temperatures: 10 K (\bullet), 30 K (\diamond), 70 K (\blacktriangle), and 90 K (Δ).

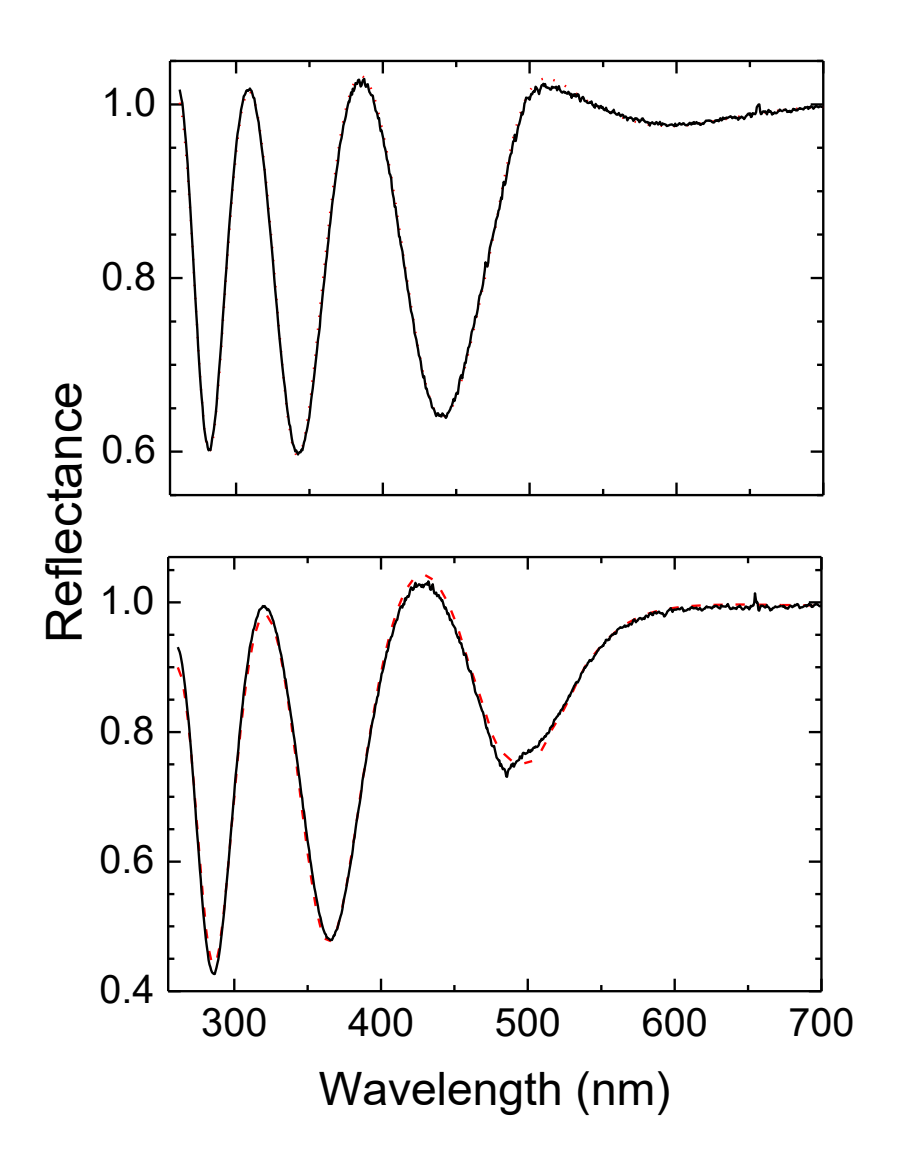


Figure 4. UV-Vis reflectance spectra (solid lines) of a 1.68 x 10^{18} H₂O cm⁻² sample background deposited at 30 K before (top) and after (bottom) irradiation with 5 keV electrons at 30 K to a fluence of 3.18 x 10^{16} electrons cm⁻². The dashed lines are the theoretical fit to the experimental data.

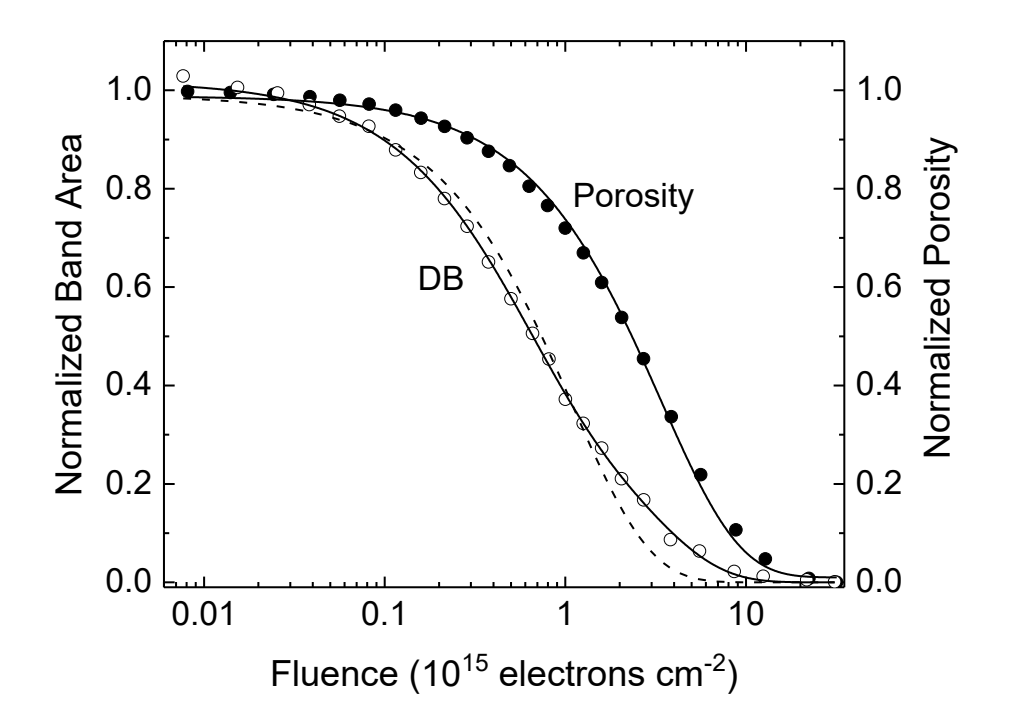


Figure 5. Normalized total area of the dangling bond absorptions (\circ) and porosity (\bullet) vs. electron fluence for a 1.68 x 10¹⁸ H₂O cm⁻² sample background deposited at 30 K and irradiated with 5 keV electrons at 30 K. The lines correspond the modeling fits to the data: solid lines are best fit models to the data, while the dashed line shows a single exponential fit to the dangling bond band area data.

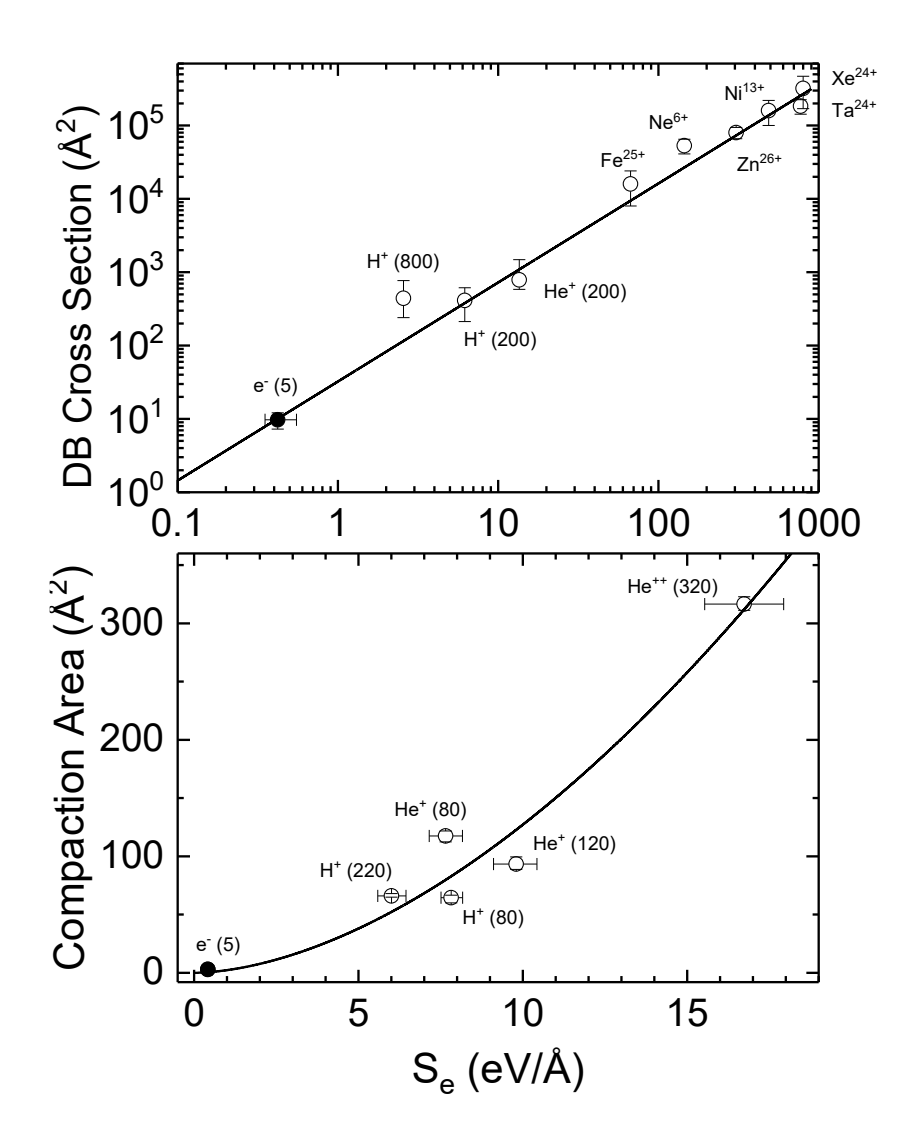


Figure 6. Top: cross section for dangling bond destruction at 30 K derived from Figure 5 (\bullet) compared with values given in Dartois et al. (2013). Cross sections given in Dartois et al. (2013) obtained from other studies are 800 keV H⁺ (Moore & Hudson 2000), 200 keV H⁺ (Palumbo 2006) and 200 keV He⁺ (Gomis, Leto, & Strazzulla 2004). Bottom: cross section for compaction of H₂O-ice at 30 K derived from Figure 5 (\bullet) compared with values obtained for light ions (\circ ; Raut et al. 2008). In both cases, the solid lined are fits to the data using an equation of the form σ = aS_e^x with the top figure corresponding to a = 32 and x = 1.35 and the bottom figure corresponding to a = 2.3 and x = 1.74.

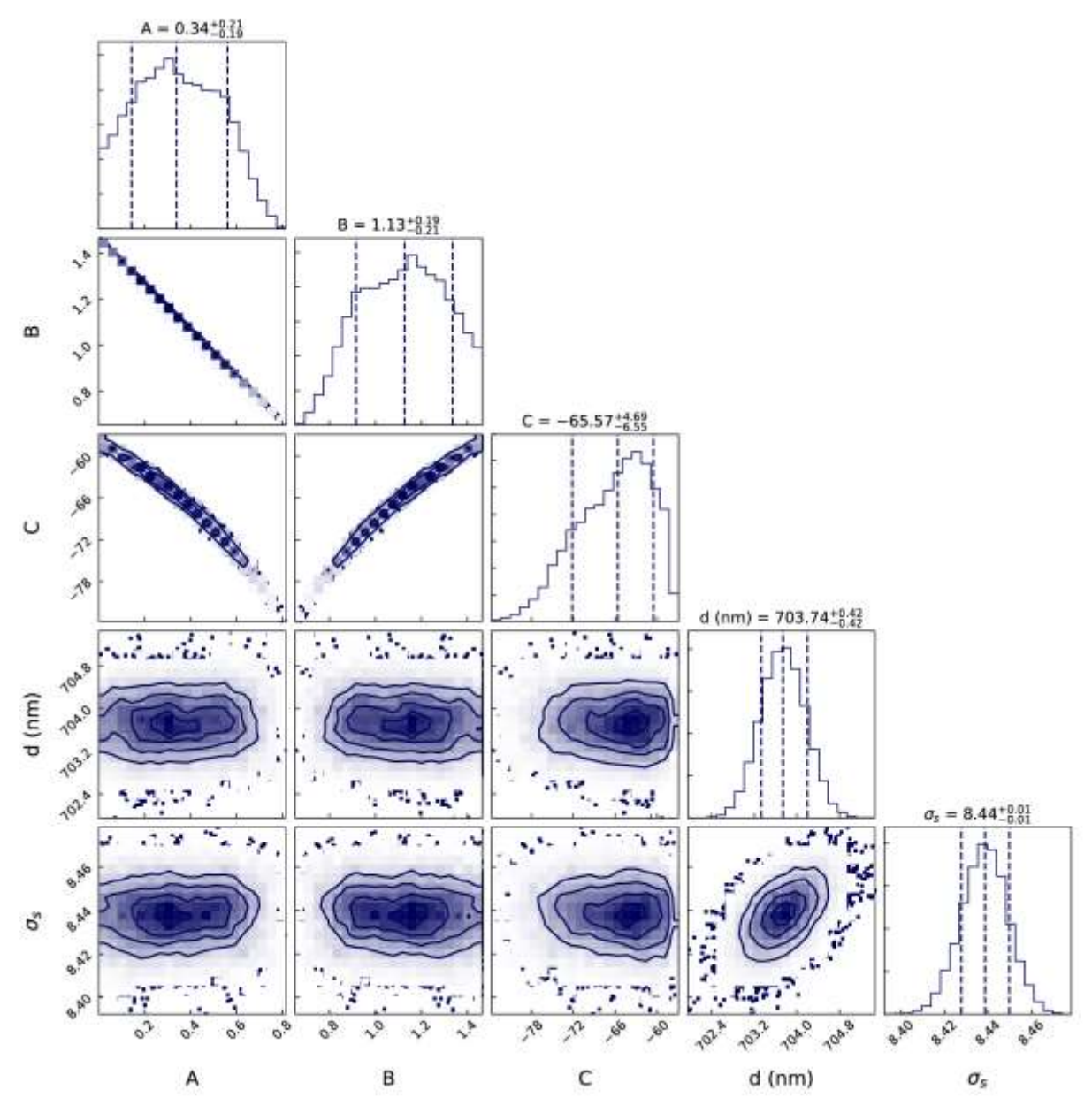


Figure 7. A typical Corner plot obtained during analysis of our UV-Vis reflectance spectra shown in Figure 4. The images show the posterior probability distributions and relation between our varied parameters: A, B and C from the Sellmeier fit, thickness and the scattering factor. See text for more details.

Table I – Estimated Energy Transfer

Variable	Units	Initial	Final	Average
¹ E	keV	5	2.71	3.93
² S _e	eV $\rm \mathring{A}^2$ / $\rm H_2O$	11.3	17.6	13.4
³ dE/dx	eV / Å	0.35	0.55	0.42
Absorbed Dose / (10 ¹⁵ electrons)	eV / H₂O			1.36

- ¹Final and average energy were calculated from an iterative program described in Loeffler et al. (2020).
- ²Estimated by taking an average of calculations made by (Ashley 1982; Berger et al. 2005; Francis et al. 2011).
- ³Assuming density of 0.94 g cm⁻³ for compact H₂O-ice (Narten et al. 1976).

T (K)	Aı	σ ₁ (Å ²)	A_2	σ ₂ (Å ²)	P ₀	σ _c (Ų)	1/e [*]
¹ 10	0.46	38.2	0.54	5.61	_	_	12.4
¹ 30	0.27	54.9	0.72	7.04	_	_	10.4
(background deposit) ² 30	0.57	20.0	0.45	3.83	_	_	9.71
(background deposit)	_	_	_	_	0.98	2.96	2.97
¹ 50	0.32	41.8	0.68	7.27	_	_	11.6
¹ 70	0.14	61.3	0.84	7.04	_	_	8.25
¹ 90	0.11	47.6	0.89	4.52	_	_	5.24

Each entry is for a least-squares fit of the data using equation $(4)^1$ and $(5)^2$.

*The values in this column are 1/F, where F is the fluence when the DB absorption has dropped by 63.2% (1/e).

Table III – Model Free Parameters

Variable	Description	Priors
Α	Sellmeier	A > 0
В	Sellmeier	B > 0
С	Sellmeier	-200 > C > 200
d	Film Thickness	d > 0
σs	Scattering Efficiency Factor	$9 > \sigma_s > 7$

Table III. Model free parameters retrieved with the reflectance model and emcee.
Physical descriptions and prior limits are additionally included.